Journal of Functional Materials and Applied Engineering

Research Paper

Antibacterial Polymer Hydrogel Based on Cold Plasma-Activated Water for Infected Wound Regeneration

Benjamin Carter[1,*], Ava Mitchell[1]

[1] Faculty of chemical engineering, Swinburne University of Technology, Hawthorn, Vic, 3122, Australia
*Corresponding author: Carter@swin.edu.au; AvaMitche@swin.edu.au

Abstract. Developing novel wound dressings with both high-efficiency antibacterial and pro-healing properties is of great significance for promoting the healing of bacterially infected wounds. In this study, a novel plasma-activated hydrogel (PAH) wound dressing was developed by substituting traditional deionized water with plasma-activated water (PAW) as the solvent during the free-radical copolymerization of acrylamide (AM) and N-acryloyl phenylalanine (APhe). The reactive oxygen/nitrogen species (RONS) enriched in PAW endowed the hydrogel with excellent antibacterial properties. Meanwhile, the unique three-dimensional network structure and abundant functional groups of the hydrogel provided an ideal matrix for the stable loading of RONS. The hydrogel exhibited mechanical properties similar to those of skin tissue (Young's modulus: 15.2 kPa, breaking strength: 198 kPa, elongation at break: 1550%), appropriate tissue adhesion (adhesive strength: 6.96 kPa), and favorable biocompatibility. It also demonstrated high-efficiency inhibition against Staphylococcus aureus(S. aureus) and Escherichia coli(E. coli), meeting the critical requirements for infected wound dressings. Furthermore, the hydrogel exhibited significant therapeutic effects on S. aureus-infected skin wounds in a murine model.

Keywords: *Hydrogel; Cold plasma-activated water; Wound dressing; Antibacterial*

Received on 02 June 2025, Accepted on 02 August 2025, Published on 15 September 2025

1 Introduction

As the largest immune organ on the body surface, the skin plays a pivotal role in maintaining the barrier function of the organism. However, skin damage caused by trauma significantly increases the risk of microbial infection[2]. Following bacterial invasion, wounds are prone to persistent exudate accumulation and dysregulated inflammation, which delay the wound healing process and severely impair patient health and quality of life[3]. Since its advent in the 1950s, antibiotics have long been regarded as the core strategy for controlling bacterial infections. Nevertheless, the overuse of antibiotics has led to increasingly severe bacterial resistance, further exacerbating public health challenges[4].

Hydrogels possess tissue-like three-dimensional networks[5]and are widely applied in the field of wound repair due to their high water content, high oxygen permeability, and good biocompatibility[6,7]. Addressing the clinical needs for infected wound treatment, current designs for antibacterial hydrogels primarily follow three technical strategies: (1) Intrinsic antibacterial polymer systems[8], which achieve antibacterial effects by introducing cationic polymers to alter bacterial membrane permeability. Gao et al. developed a hyperbranched polylysine composite hydrogel that exhibited excellent antibacterial performance against S. aureusand accelerated the wound healing process. However, this system suffers from limitations such as a narrow antibacterial spectrum and declining long-term antibacterial efficacy. (2) Functional component loading, such as metallic particles[9]or antibacterial drugs[10]. Cheng et al.[11]loaded silver nanoparticles into a polyvinyl alcohol/konjac glucomannan/borax hydrogel. The nanoparticles inhibited bacterial replication by binding to ATP synthase in the cell wall or blocking the respiratory chain within bacteria, thereby achieving antibacterial effects. However, this approach readily induces the generation of drug-resistant strains, and the aggregation of

nanoparticles in vivomay lead to potential biotoxicity. (3) Physical field-responsive synergistic therapy, which achieves precise antibacterial action through external energy modulation[12]. Liu et al.[13]developed an immunoinducible carbon dot-incorporated hydrogel that achieved a high bacterial inactivation rate under near-infrared irradiation. However, this strategy relies on high temperatures to directly destroy microbial structures, which can easily cause thermal damage to surrounding tissues. Therefore, constructing hydrogel dressings with high-efficiency antibacterial properties and no drug resistance remains an urgent problem to be solved.

Cold atmospheric plasma (CAP) is a partially ionized gas generated by electrical discharge under ambient temperature conditions, known as the fourth state of matter. Through the interaction between CAP and deionized water induced by a high-voltage electric field, abundant reactive nitrogen species (RNS) and reactive oxygen species (ROS)—such as long-lived particles including O_3, H_2O_2, and NO_2^-, as well as short-lived particles like ·O, ·OH, and ·NO—can be produced[15]. The resulting plasma-activated water (PAW) exhibits multiple biological effects; it can not only disrupt microbial membrane integrity via ROS-mediated oxidative damage but also induce cancer cell apoptosis via RNS-mediated DNA damage. Notably, PAW demonstrates broad-spectrum antibacterial activity without inducing microbial resistance[16]. Consequently, PAW shows broad application potential in medical fields such as disinfection and the regulation of cancer cell apoptosis[17]. However, the short half-life of RONS in PAW leads to rapid attenuation of its antibacterial activity, severely restricting its clinical application. In contrast, the three-dimensional network structure and abundant functional groups of hydrogels provide an ideal matrix for the stable loading of RONS. The Zhang team (Liu et al.) prepared a polyacrylamide hydrogel using PAW instead of deionized water and confirmed that its antifungal activity duration was significantly extended compared to PAW alone. However, the poor mechanical properties of this material limit its further application as a wound dressing.

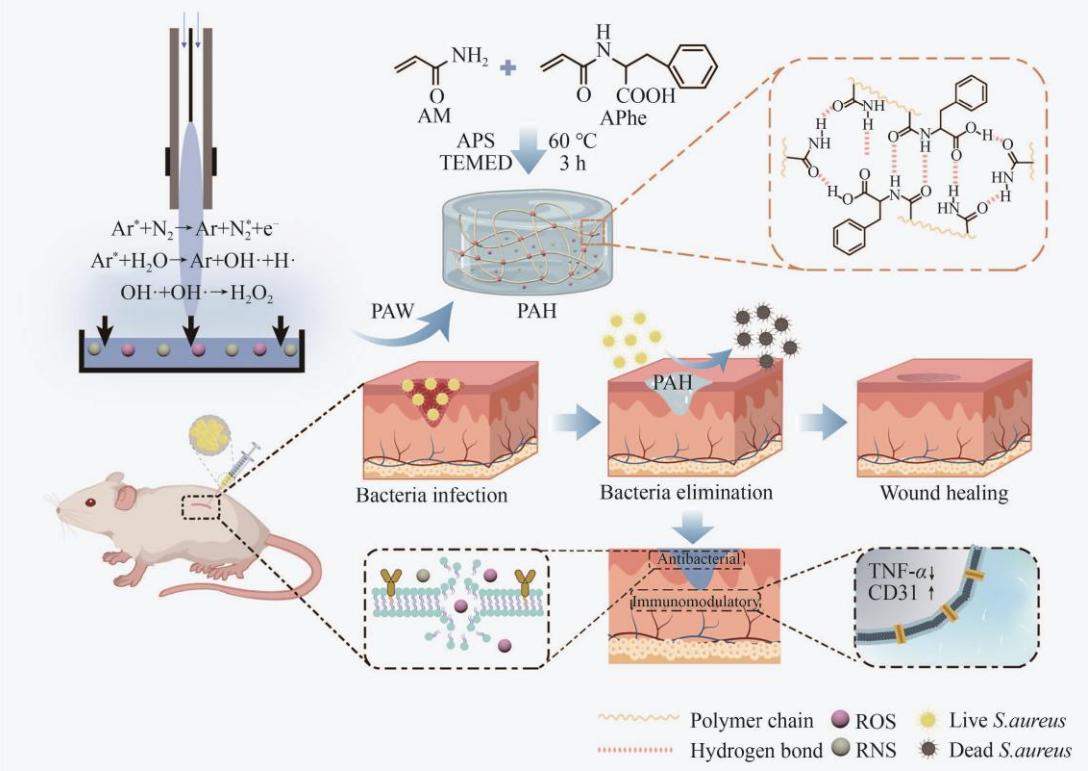

Figure 1 Schematic diagram of the preparation of PAH and its application in promoting the healing of infected skin wounds.

In our previous study[19], a hydrogel material with excellent mechanical properties was developed via the free-radical copolymerization of AM and the amino acid derivative APhe. In this system, multiple hydrogen bonds can form between APhe-APhe or APhe-AM, constructing stable non-covalent cross-linking points within the polymer network and promoting gelation. Building on this foundation, the present study utilized PAW as a

reaction solvent to replace deionized water, constructing a novel plasma-activated hydrogel (PAH). We systematically evaluated its mechanical properties, tissue adhesion, in vitroantibacterial activity, and biocompatibility (Fig. 1). Furthermore, using a murine full-thickness skin defect model infected with S. aureus, we further assessed its in vivoantibacterial performance and wound healing-promoting capability.

2 Experimental Section

2.1 Instruments and Reagents

CTK-2000K low-temperature plasma experimental power supply (Nanjing Summan Electronics Co., Ltd.); D08-4F flow rate display instrument (Beijing Sevenstar Huachuang Flowmeter Co., Ltd.); LGJ-12A vacuum freeze dryer (Beijing Sihuan Qihang Technology Co., Ltd.); Infinite 200 PRO microplate reader (Tecan, Switzerland); CMT-1503 universal electronic tensile testing machine (Sans Testing Machine Co., Ltd.); AVANCE 400 nuclear magnetic resonance spectrometer (NMR, Bruker, USA); SU3500 tungsten filament scanning electron microscope (SEM, Hitachi, Japan); DMi8 inverted fluorescence microscope (Leica, Germany).

L-Phenylalanine (L-Phe, reagent grade) and AM (reagent grade) were purchased from Shanghai Admas Reagent Co., Ltd.; Ammonium persulfate (APS, reagent grade) from Sigma-Aldrich Trading Co., Ltd. (Shanghai); Tetramethylethylenediamine (TEMED, reagent grade) from Shanghai Aladdin Biochemical Technology Co., Ltd.; H_2O_2 assay kit, Griess assay kit, and 3-(4,5-dimethylthiazol-2-yl)-2,5-diphenyltetrazolium bromide (MTT) from Solarbio Science & Technology Co., Ltd.; Cell viability and cytotoxicity assay kits from Beyotime Biotechnology; Mouse fibroblasts (L929), DMEM high-glucose medium, and phosphate-buffered saline (PBS) from Wuhan Pricella Life Science Co., Ltd.

2.2 Experimental Methods

2.2.1 Preparation of PAW

Argon (Ar) was used as the working gas at a flow rate of 1 SLM to activate deionized water using a cold plasma jet mode. The experimental ambient temperature was maintained at 25 °C, with a relative humidity of 40%–50%. The input voltage and frequency of the plasma power supply were 220 V and 50 Hz, respectively, with an output voltage and frequency of 5 kV and 20 kHz. The activation setup employed a vertically fixed jet electrode. A glass dish containing 20 mL of deionized water was placed beneath the jet nozzle, with the liquid surface adjusted to 10 mm below the nozzle for activation over different durations.

2.2.2 Preparation of PAH

AM (426 mg) and APhe (15.8 mg) were completely dissolved in 2 mL of PAW. N_2 bubbling was performed for 5 min to remove oxygen. A thermal initiator, APS (1 wt% relative to monomer mass), and an accelerator, TEMED (0.3 wt% relative to monomer mass), were added and mixed thoroughly. Polymerization was conducted at 60 °C for 3 h to obtain PAH-x, where xrepresents the PAW activation time. The feed ratio of AM to APhe referred to our previous work[19].

The preparation of deionized water hydrogel (DWH) followed a similar procedure, except that PAW was replaced with deionized water (DW).

2.2.3 Characterization and Performance Testing

2.2.3.1 In VitroAntibacterial Performance Evaluation

The in vitroantibacterial efficacy of PAH was evaluated using the dilution plate coating method. S. aureusand E. coli(10 µL each) were inoculated into LB liquid medium (10 mL) and cultured in a thermostatic shaking incubator at 37 °C and 120 r/min for 12 h. After centrifugation, the bacterial pellet was resuspended in sterile PBS. 200 mg of PAH-xwas placed in a 24-well plate; the control group received 200 µL of sterile PBS. Each experimental group comprised three replicates. The 24-well plate was sterilized under UV light for 30 min to prevent interference from contaminants. 10 µL of bacterial suspension (10^6 CFU/mL) was added to each well, followed by co-culture

in a constant temperature incubator at 37 °C for 6 h. Subsequently, 1 mL of sterile PBS was added to each well to resuspend the surviving bacteria. 100 µL of the bacterial suspension from each well was evenly spread onto LB agar plates and cultured for another 12 h. Colonies on the agar plates were counted using Image J software. The bacterial survival rate (BV) was calculated according to Formula (1):

$$B_V = \frac{B_S}{B_C} \times 100\% \quad (1)$$

where BS and BC represent the number of surviving bacteria in the experimental group and the control group, respectively.

2.2.3.2 Evaluation of Infected Wound Healing Promotion

All animal experiments were approved by the Ethics Committee of Xi'an Jiaotong University and complied with all applicable regulations and ethical guidelines. Male Kunming mice (approximately 40 g) were used to establish a full-thickness skin defect infection model to evaluate the therapeutic effect of PAH on infected wounds. Under general anesthesia induced by sodium pentobarbital (50 mg/kg), a 10 mm full-thickness skin incision was created on the back of each mouse, followed by injection of 20 µL of S. aureus(1×10^7 CFU/mL) into the wound site to establish infection. All infected mice were randomly divided into four groups for intervention: ① Blank control group, treated simply with PBS; ② Tegaderm™ group, covered with sterilized commercial Tegaderm™ film; ③ DWH group, covered with sterilized DWH; ④ PAH-20 group, covered with sterilized PAH-20. One day post-treatment, three mice were randomly selected from each group to collect skin tissue from the wound site. The tissue was homogenized in 1 mL of sterile PBS. 100 µL of the tissue homogenate was spread onto LB agar plates, cultured at 37 °C for 12 h, and colonies were counted using Image J software. Digital images of the wounds were recorded on days 7 and 14 post-treatment. Wound tissues were harvested for hematoxylin and eosin (H&E) staining, Masson's trichrome staining, and immunofluorescence staining for histopathological analysis.

3 Results and Discussion

3.1 Preparation and Physicochemical Property Analysis of PAW

As shown in Fig. 2A, PAW was generated using a cold plasma jet mode. The voltage waveform in Fig. 2B exhibits typical sinusoidal characteristics, indicating that the system operated in a stable alternating current state during preparation. The sharp current peaks occurring at voltage zero-crossings confirm the generation of reactive species in the plasma, resulting in transient high ionization. Optical emission spectroscopy (OES) was further employed to analyze reactive species in the gaseous plasma. Fig. 2C depicts the optical emission spectrum across a wavelength range of 200–900 nm, primarily composed of the first negative band of N2+ (B2Σu+ →X2Σg+), the second positive band of N2 (C3Πu+ →B3Πg), and the secondary diffraction of N2 (C3Πu→B3Πg). The N2 (C3Πu →B3Πg) transition is formed via electron impact on ground-state N2 (X2Σg+), while the first metastable state N2 (A3Σg+) and N2+ (B2Σg+) are formed via direct bombardment by high-energy electrons. Consequently, nitrogen and oxygen in the air were excited, generating biologically active reactive oxygen/nitrogen species (RONS).

Further physicochemical analysis of PAW was conducted. When the plasma treatment time was extended to 30 min, the pH of the system decreased significantly from an initial 7.04 to 3.94 (Fig. 2D), attributable to acidification induced by plasma-generated reactive species[14]. The oxidation-reduction potential (ORP) also increased synchronously with treatment time, rising from 231 mV to 422 mV (Fig. 2E), demonstrating a positive correlation between oxidative capacity and treatment duration. Concurrently, reactive species generated during plasma treatment significantly enhanced the electrical conductivity of the solution (Fig. 2F). To clarify the concentrations of key active components in PAW, detection kits combined with fluorescence emission spectroscopy were used to establish standard curves for quantitative analysis (Fig. S1 in Supporting Information). The results indicated that the concentrations of active species such as H_2O_2, NO_2^-, and ·OH all exhibited a positive correlation with plasma treatment time (Fig. 2G–2I).

DOI:

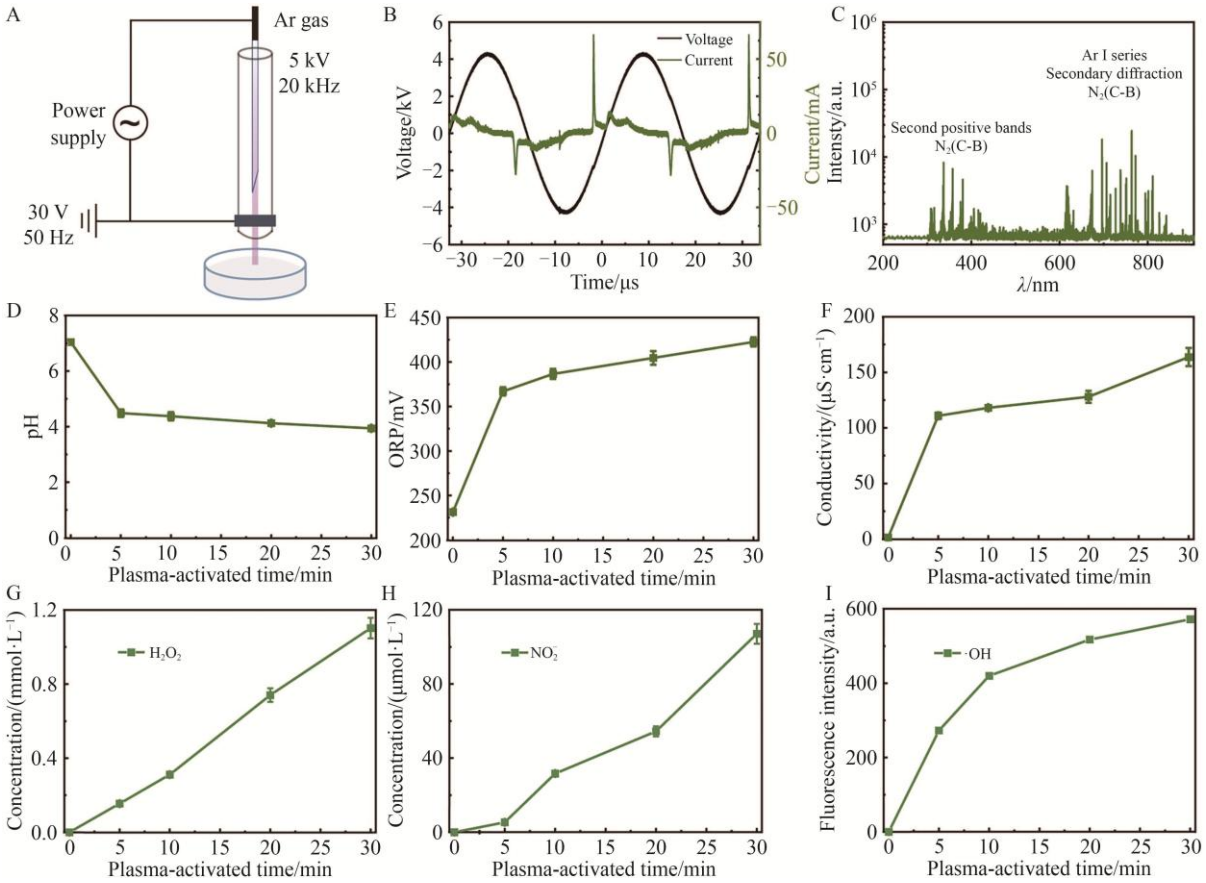

Figure 2 Preparation and physicochemical properties analysis of PAW. (A) Illustration of the mechanism for PAW generation; (B) Waveforms of discharge current and voltage; (C) Emission spectra of the cold plasma jet discharge; Variation of pH (D), ORP (E), and conductivity (F) of PAW with plasma-activated durations; Variation of H_2O_2 (G), NO_2^- (H), and ·OH (I) concentrations in PAW with plasma-activated durations.

Subsequently, PAH was constructed via the free-radical copolymerization of AM and the amino acid derivative APhe using PAW as the reaction solvent instead of deionized water. ^{1}H NMR spectra (Fig. S2 in Supporting Information) revealed that the molar ratio of AM to APhe in PAH was 2.94:0.04, roughly consistent with the feed ratio, and the monomer conversion rate reached 99%, confirming the successful synthesis of PAH.

3.2 In Vitro Antibacterial Performance Evaluation of PAH

During skin injury repair, bacterial infection not only exacerbates wound deterioration and delays healing but also induces severe complications. Therefore, effective control of bacterial infection is crucial for promoting wound healing. In this study, E. coliand S. aureuswere employed as representative models of Gram-negative and Gram-positive bacteria, respectively, to evaluate the in vitroantibacterial performance of PAH. The experimental results showed that DWH without activation exhibited almost no inhibitory effect on either pathogen, showing no significant difference from the blank control group (Fig. 3A). As the activation time increased, the antibacterial performance of PAH gradually improved. The antibacterial efficiency of PAH was quantified by counting colony-forming units (CFUs) on the culture media. As shown in Fig. 3B, after 20 min of activation, PAH achieved antibacterial efficiencies exceeding 99.9% against both E. coliand S. aureus. These results indicate that PAH possesses broad-spectrum antibacterial activity, exerting significant inhibitory effects on both Gram-negative and Gram-positive bacteria. The antibacterial mechanism is primarily attributed to the abundance of RONS in PAH, particularly components like H_2O_2, which disrupt bacterial membrane integrity via oxidative damage and alter osmotic pressure homeostasis, ultimately leading to microbial death. When the activation time was extended to 30 min, no further significant enhancement in the antibacterial performance of PAH was observed; therefore, PAH-20 was selected for subsequent experiments.

To further evaluate the long-acting antibacterial activity of PAH, the antibacterial efficiencies of PAW-20 and PAH-20 were compared after different storage periods. The results revealed (Fig. 3C) that during a 3-day storage period, the antibacterial activities of both remained comparable. However, when the storage time was extended to 10 days, PAW-20 completely lost its antibacterial capacity due to the decay of active components. In contrast, benefiting from the stable loading and sustained-release characteristics of the three-dimensional network structure for active substances, PAH-20 maintained an antibacterial efficiency above 90% (Fig. 3D and 3E). Further verification via active substance detection confirmed that after 30 days, the concentration of H_2O_2 in PAH remained at approximately 34% of its initial level, significantly higher than that in PAW, substantiating the hydrogel system's capacity for sustained release and stabilization of active substances, which corroborates its long-acting antibacterial performance (Fig. S3 in Supporting Information). However, although PAH effectively prolongs the lifetime of RONS, it cannot completely inhibit their spontaneous decomposition; with prolonged storage, the RONS in PAH will eventually be depleted over time.

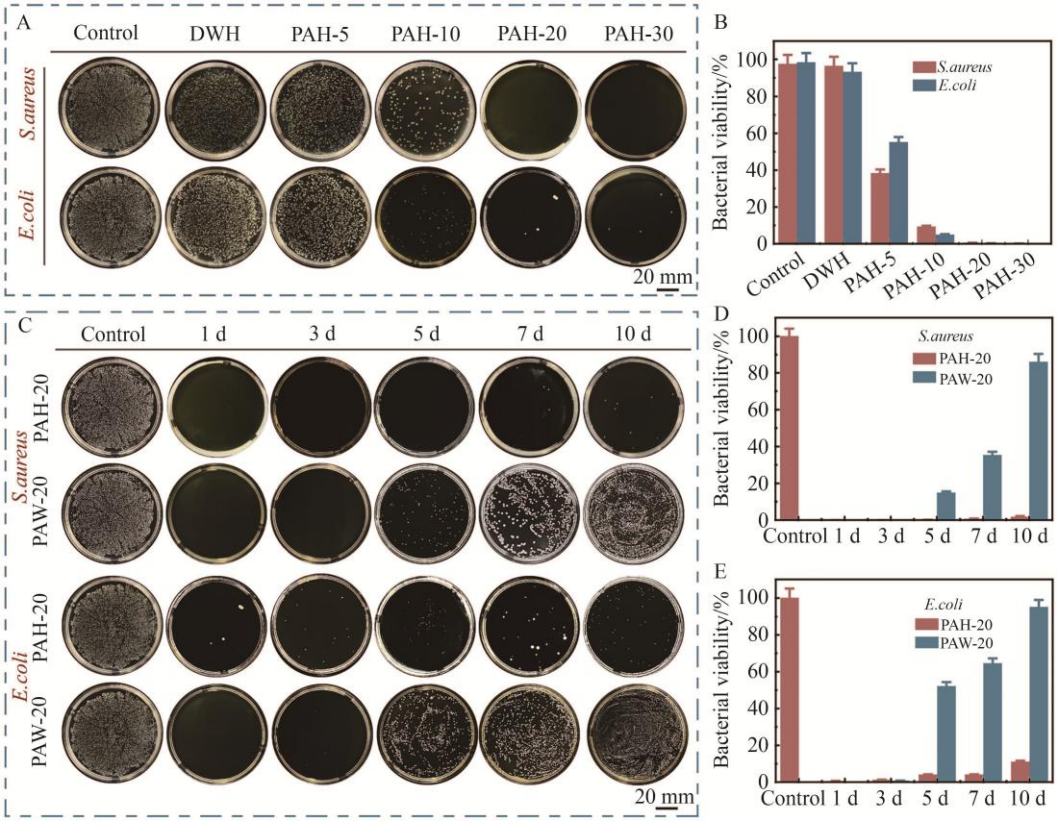

Figure 3 In vitroantibacterial properties of PAH. Photographs of surviving bacteria on agar plates (A) and relative bacterial survival rates of S. aureusand E. coli(B) after co-culturing with PAH-20; Photographs of surviving bacteria on agar plates (C) and relative bacterial survival rates of S. aureus(D) and E. coli(E) after co-culture with PAH-20 and PAW-20 stored for 1, 3, 5, 7, and 10 days.

3.3 Mechanical and Adhesive Properties Evaluation of PAH-20

An ideal wound dressing should possess mechanical properties matching those of skin tissue. In this study, uniaxial tensile (Fig. 4A) and compression tests (Fig. 4B) were conducted to evaluate the mechanical properties of PAH-20. Compared with DWH, plasma activation treatment caused a slight decrease in Young's modulus, tensile strength, and compressive strength of the hydrogel, while significantly increasing its elongation at break (Fig. 4C). This phenomenon is speculated to arise because RONS in PAW may interfere with the free-radical polymerization process, leading to the quenching of short-lived free radicals and reduced termination efficiency of molecular chains, thereby forming longer polymer chains[29]. The expanded spacing between cross-linking points loosens the network structure, consequently affecting the mechanical properties of the hydrogel. To verify this hypothesis, the microstructure of the hydrogels was observed via SEM. As shown in Fig. 4D and 4E,

both PAH-20 and DWH exhibited three-dimensional interconnected porous network structures; however, the structure of PAH-20 was relatively looser, with an average pore diameter ((3.43±1.43) μm) higher than that of DWH ((2.01±0.82) μm), indicating a lower cross-linking density (Fig. 4F). The loose porous network structure of PAH-20 can absorb tissue exudate and permit oxygen permeation, while providing ample space for cell attachment and proliferation. Furthermore, the Young's modulus of PAH-20 (15.2 kPa) closely matches that of skin tissue, and its high stretchability effectively reduces skin tension at the wound site, thereby preventing the formation of scar tissue. These characteristics collectively provide favorable conditions for the rapid healing of skin wounds.

Moderate tissue adhesion is another critical feature of an ideal wound dressing[9]. Experiments demonstrated that PAH-20 could firmly adhere to visceral tissues (stomach, spleen, liver, heart, and lungs) of mice and various organic/inorganic material surfaces (Fig. 4G). Quantitative lap-shear test results (Fig. 4H) showed that the adhesive strength of PAH-20 to glass, iron sheets, and porcine skin was approximately 8.02, 12.19, and 6.76 kPa, respectively. Notably, its adhesive strength to porcine skin surpassed that of the currently commercial fibrin glue (Greenplast®)[20]. The adhesion of PAH-20 can be attributed to non-covalent interactions formed between the hydrogel and different substrates[20], facilitating stable attachment and continuous protection of the wound site, thereby accelerating the wound healing process.

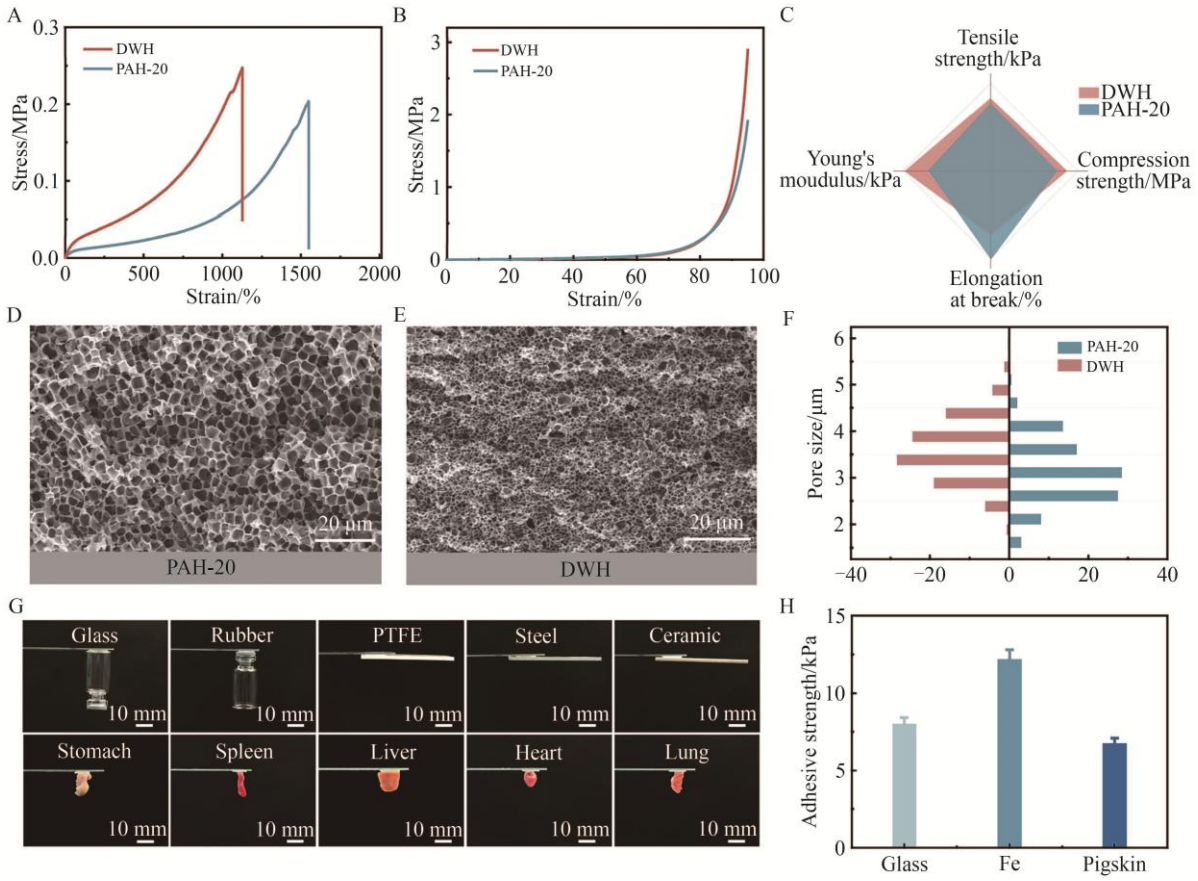

Figure 4 Mechanical properties and adhesive properties of PAH-20. Tensile (A) and compressive (B) stress-strain curves and mechanical properties comparison radar chart (C) of PAH-20 and DWH; SEM images of PAH-20 (D) and DWH (E) and pore diameter statistics (F); (G) Photos of PAH-20 adhered to different substrate surfaces; (H) Adhesion strengths of PAH-20 with different substrates.

3.4 Biocompatibility Evaluation of PAH-20

Biocompatibility is a core criterion for the clinical application of biomedical materials[7]. First, the hemocompatibility of the hydrogel was evaluated via an in vitrohemolysis assay. Triton X-100 and PBS served as

the positive and negative controls, respectively. As shown in Fig. S4 in Supporting Information, no obvious hemoglobin release was observed in the DWH or PAH-20 groups; the supernatants were transparent and showed no significant difference from the negative control group. In contrast, the positive control group exhibited extensive erythrocyte rupture due to cell membrane lysis, resulting in a bright red supernatant. Further quantification of the hemolysis rate revealed that the hemolysis rates of both the DWH and PAH-20 groups were below 5%, meeting the international clinical application threshold[21], thus confirming their good hemocompatibility. Subsequently, the cytocompatibility of the hydrogel was evaluated using the MTT assay and live/dead cell staining. As shown in Fig. S5 in Supporting Information, after co-culture with extracts from DWH and PAH-20 for different durations, the cell viability and proliferation ability of L929 cells in all hydrogel groups showed no significant difference from the blank control group (DMEM medium). Fluorescence staining results revealed that L929 cells treated with DWH and PAH-20 were almost entirely stained green (live cells), with morphologies and proliferation trends consistent with the control group (Fig. S5), further indicating their excellent cytocompatibility. Comprehensive results demonstrate that PAH-20 meets the biocompatibility requirements for medical materials.

3.5 Evaluation of PAH-20 in Promoting Healing of Infected Skin Wounds

Based on the excellent antibacterial performance and good biocompatibility of PAH-20, it holds promise for further application as a wound dressing. S. aureusis one of the most common pathogens in wound infections[22]; therefore, a murine skin wound model infected with S. aureuswas established to meticulously evaluate the therapeutic effect of PAH-20 (Fig. 5A). Fig. 5B presents macroscopic photographs of the wounds at different time points. On postoperative day 7, the wound area in the PAH-20 group was significantly reduced, with a healing efficiency (25.7%) markedly higher than that of the control group (4.8%), Tegaderm™ group (6.6%), and DWH group (9.2%) (Fig. 5C).

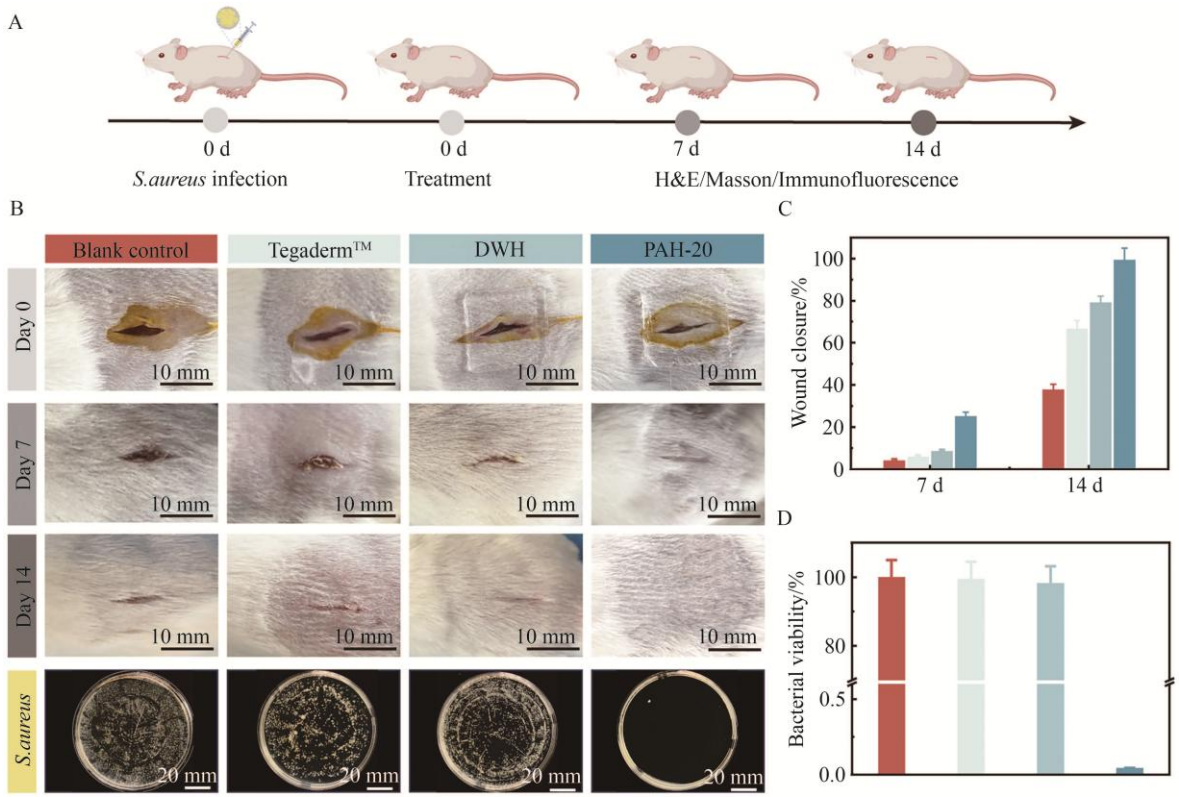

Figure 5 Evaluation of healing capability of PAH-20 in promoting infected wounds. (A) Schematic diagram of infected wound model and treatment; (B) Macroscopic photos of infected wound closure and bacterial colonies in subcutaneous tissue in different treatment groups; (C) Wound closure in different groups; (D) Quantitative bacterial survival rate of S. aureusextracted from different treatment groups.

This is attributed to the effective inhibition of bacterial growth by RONS in PAH-20, significantly shortening the inflammatory cycle and accelerating the tissue regeneration process. On postoperative day 14, the wound in the PAH-20 group was fully epithelialized and covered with newly grown hair, whereas obvious unhealed areas remained in the other groups, fully demonstrating the advantages of PAH-20 in promoting wound closure and tissue regeneration. To quantitatively assess the in vivoantibacterial efficacy of PAH-20, skin tissues from the treatment sites were collected, homogenized, and cultured on agar plates. As shown in Fig. 5B, almost no bacterial infection was detectable in the PAH-20 group, with a bacterial survival rate of less than 1% (Fig. 5D). The aforementioned results indicate that PAH-20 can efficiently clear wound bacteria and significantly accelerate the wound healing process, exhibiting unique advantages in the treatment of infected wounds.3.6 Histological Analysis of PAH-20 Promoting Healing of Infected Skin Wounds

The healing of infected wounds follows the sequential stages of hemostasis, inflammation, proliferation, and remodeling[23]. During the inflammatory phase, macrophages and T lymphocytes significantly promote the production of tumor necrosis factor-alpha (TNF-α)[24]. After inflammation subsides, endothelial cell activation and the ensuing neovascularization ensure adequate oxygen and nutrient supply for the nascent tissue[25].

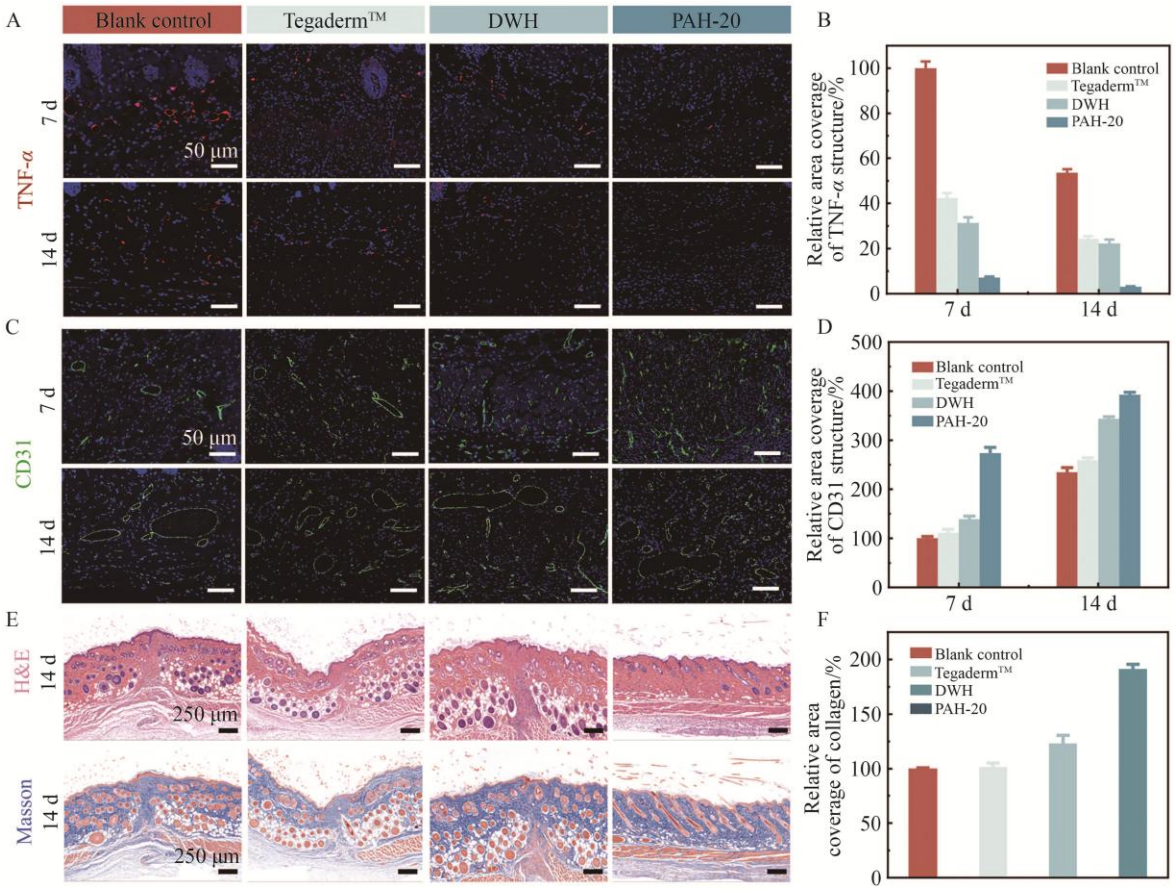

Figure 6 Fig. 6 Histological analysis of PAH-20 promoting wound healing in skin infection. Immunofluorescence staining (A) and semi-quantitative analysis (B) of TNF-α in wound tissue after 7 and 14 days of treatment; Immunofluorescence staining (C) and semi-quantitative analysis (D) of CD31 in wound tissue after 7 and 14 days of treatment; (E) H&E and Masson staining of wound tissue after 14 days of treatment; (F) Semi-quantitative analysis of collagen deposition in wound tissue after 14 days of treatment.

In this study, immunofluorescence staining was employed to detect the expression levels of the pro-inflammatory factor TNF-α and platelet endothelial cell adhesion molecule-1 (CD31), systematically evaluating the effects of PAH-20 on inflammation regulation and angiogenesis. On postoperative day 7 (Fig. 6A and 6B), damaged tissues in the control group remained in a state of exacerbated inflammation, whereas the

inflammatory response in the PAH-20 group was significantly reduced, with diminished TNF-α expression, effectively curbing the inflammatory response triggered by excessive macrophage activation. Concurrently, the density of CD31-labeled neovessels in the PAH-20 group was significantly higher than that in the other groups, confirming that PAH-20 accelerates angiogenesis by activating endothelial cells (Fig. 6C and 6D). On postoperative day 14, the inflammatory response in all groups had markedly weakened, with significantly decreased TNF-α expression levels. The wound in the PAH-20 group was nearly completely healed, and the angiogenesis status was superior to that in the other control groups. The above results indicate that PAH-20 effectively promotes wound healing by downregulating TNF-α expression and upregulating CD31 expression.

Further evaluation of the wound healing progression in different treatment groups was conducted via hematoxylin and eosin (H&E) staining. On postoperative day 14, the PAH-20 group exhibited almost no inflammatory cell infiltration and formed a continuous, intact epithelial structure compared to the other control groups. During the remodeling phase, collagen fiber deposition is crucial for the formation of the new connective tissue matrix[26]. Therefore, Masson's trichrome staining was performed to measure collagen deposition and assess the reparative effects in different treatment groups. As shown in Fig. 6E and 6F, compared with the control, Tegaderm™, and DWH groups, collagen deposition in the PAH-20 treatment group was denser, indicating its favorable pro-repair effect on skin wounds. Integrating the aforementioned results, PAH-20 can, through its sustained antibacterial action, promptly clear pathogens in the early stages, shorten the inflammatory response, promote the premature entry of the wound into the proliferative phase, and thereby accelerate the repair of infected skin wounds.

4 Conclusion

By substituting PAW for deionized water as the solvent in the free-radical copolymerization system of AM and APhe, a novel plasma-activated hydrogel wound dressing was developed. The RONS enriched in PAW endowed the hydrogel with excellent antibacterial properties, effectively inhibiting the growth of S. aureusand E. coli. Meanwhile, the three-dimensional network structure and abundant functional groups of the hydrogel provided an ideal matrix for the stable loading of RONS, significantly extending the antibacterial activity of PAW. The prepared PAH-20 exhibited outstanding mechanical properties, moderate tissue adhesion, good biocompatibility, and long-acting antibacterial activity, satisfying the critical performance requirements for antibacterial wound dressings. In a murine skin wound model infected with S. aureus, PAH-20 effectively reduced inflammation by inhibiting bacterial proliferation and accelerated wound healing, demonstrating superior therapeutic effects. Overall, this plasma-activated hydrogel provides a facile and efficient strategy for designing dressings for infected skin wounds, showcasing immense application potential in the treatment of infected wounds.

Supporting Information

Supporting Information: Standard curves for NO_2^- and H_2O_2 concentrations, variation of H_2O_2 concentration with storage time, hemocompatibility and cytocompatibility of PAH-20, etc.

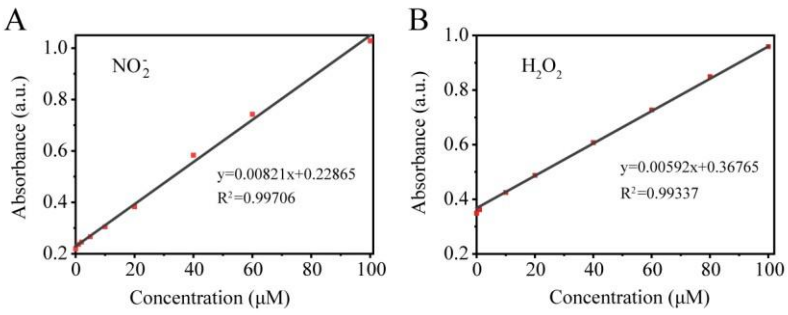

Fig. S1 (A) Standard curve of NO-2 concentration; (B) Standard curve of H2O2 concentration

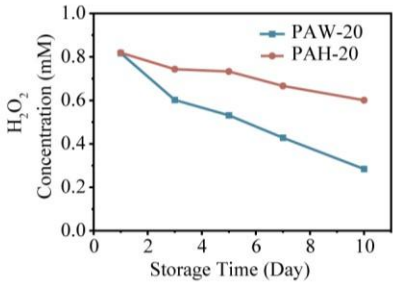

Fig. S2 Variation of H2O2 concentration in PAW-20 and PAH-20 with storage time at room temperature

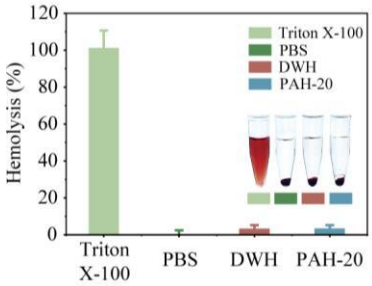

Fig. S3 Hemolysis ratio of PAH-20

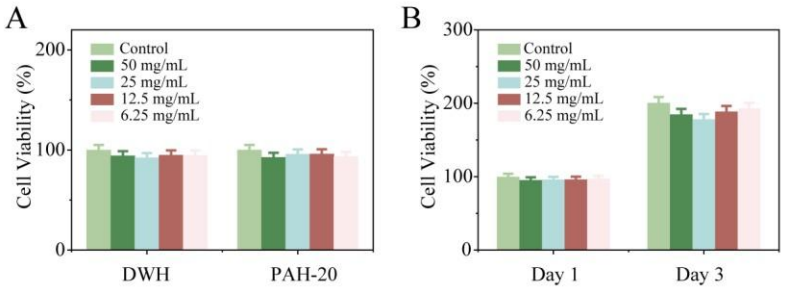

Fig. S4 (A) Cell viability of L929 after incubating with different concentration extraction of DWH and PAH-20 for 1 day; (B) Cell viability of L929 after incubating with different concentration extraction of PAH-20 for 3 days

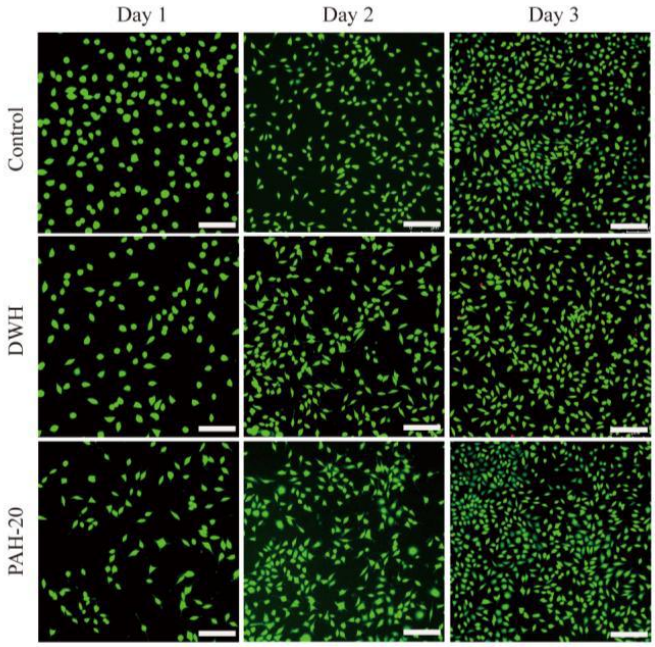

Fig. S5 Live/Dead staining images of L929 after incubating with DWH and PAH-20 for 3 days. Scale bar: 100 μm

References

[1] LIU X Q, SUN Y M, WANG J, et al. A tough, antibacterial and antioxidant hydrogel dressing accelerates wo und healing and suppresses hypertrophic scar formation in infected wounds[J]. Bioact Mater, 2023, 34: 2 69-281.

[2] DU J Q, ZHANG Y F, CHENG Y L. Construction of poly(lipoic acid)-based functional hydrogels for infected sk in wound healing[J]. Acta Polym Sin, 2024, 55(5): 624-636.

[3] XIA H, DONG Z, TANG Q, et al. Glycopeptide-based multifunctional hydrogels promote diabetic wound he aling through pH regulation of microenvironment[J]. Adv Funct Mater, 2023, 33(29): 2215116.

[4] MATHEW S, OLGA S, IDAN Y, et al. Minimizing treatment-induced emergence of antibiotic resistance in ba cterial infections[J]. Science, 2022, 375: 889-894.

[5] FU F S, CHEN H H, CHEN Y, et al. Engineered Bacillus subtilis enhances bone regeneration via immunoregu lation and anti-infection[J]. Bioact Mater, 2025, 46: 503-515.

[6] MA S B, HAN C H, CHEN X, et al. Self-healing adhesive hydrogels for sustained ozone release: enhanced an tibacterial properties and improved wound healing[J]. J Control Release, 2025, 377: 212-222.

[7] LIU Q, WANG C X, CHENG M Q, et al. Self-healing conductive hydrogels with dynamic dual network struct ure accelerate infected wound healing via photothermal antimicrobial and regulating inflammatory respo nse[J]. ACS Appl Mater Interfaces, 2024, 16(24): 30776-30792.

[8] DEY R, MUKHERJEE R, HALDAR J. Photo-crosslinked antimicrobial hydrogel exhibiting wound healing abilit y and curing infections in vivo[J]. Adv Healthc Mater, 2022, 11(15): 2200536.

[9] MENG W L, LIN Z, CHEENG X, et al. Thiourea-cation chelation based hydrogel and its application as antiba cterial dressing for the repair of diabetic wound[J]. Adv Funct Mater, 2024, 34(22): 2314202.

[10] GONG Y, WANG P, CAO R, et al. Exudate absorbing and antimicrobial hydrogel integrated with multifuncti onal curcumin-loaded magnesium polyphenol network for facilitating burn wound healing[J]. ACS Nano, 2 023, 17(22): 22355-22370.

[11] CHENG H, KEERTHIKA DEVI R, HUANG K Y, et al. Highly biocompatible antibacterial hydrogel for wearable sensing of macro and microscale human body motions[J]. Small, 2024, 20(37): 2401201.

[12] CHANG L M, CHEN Y N, ZHOU M, et al. Photothermal enhanced antibacterial chitosan-based polydopamin e composite hydrogel for hemostasis and burn wound repairing[J]. Carbohydr Polym, 2024, 345: 122568.

[13] LIU S W, ZHANG M M, YU H J, et al. Immunoinducible carbon dot-incorporated hydrogels as a photothermal-derived antigen depot to trigger a robust antitumor immune response[J]. ACS Appl Mater Interfaces, 2023, 15(6): 7700-7712.
[14] THIRUMDAS R, KOTHAKOTA A, ANNAPURE U, et al. Plasma activated water (PAW): chemistry, physico-chemical properties, applications in food and agriculture[J]. Trends Food Sci Technol, 2018, 77: 21-31.
[15] CLEMEN R, FREUND E, MROCHEN D, et al. Gas plasma technology augments ovalbumin immunogenicity and OT-II T cell activation conferring tumor protection in mice[J]. Adv Sci, 2021, 8(10): 2003395.
[16] CHEN J, WANG Z, SUN J, et al. Plasma-activated hydrogels for microbial disinfection[J]. Adv Sci, 2023, 10(14): e2207407.
[17] MAHDIKIA H, SHOKRIA B, MAJIDZADEH K. The feasibility study of plasma-activated water as a physical therapy
[18] LIU Z X, ZHENG Y P, DANG J, et al. A novel antifungal plasma-activated hydrogel[J]. ACS Appl Mater Interfaces, 2019, 11(26): 22941-22949.
[19] YU J, XU K, CHEN X J, et al. Highly stretchable, tough, resilient, and antifatigue hydrogels based on multiple hydrogen bonding interactions formed by phenylalanine derivatives[J]. Biomacromolecules, 2021, 22(3): 1297-1304.
[20] ZHANG M Y, LIN P L, SONG X F, et al. Injectable and self-healing hydrogels with tissue adhesiveness and antibacterial activity as wound dressings for infected wound healing[J]. J Polym Sci, 2022, 60(9): 1511-1520.
[21] WANG Y, WU Y, LONG L Y, et al. Inflammation-responsive drug-loaded hydrogels with sequential hemostasis, antibacterial, and anti-inflammatory behavior for chronically infected diabetic wound treatment[J]. ACS Appl Mater Interfaces, 2021, 13(28): 33584-33599.
[22] GIUDICE P. Skin infections caused by Staphylococcus aureus[J]. Acta Derm Venereol, 2020, 100(9): adv00110-00215.
[23] XIANG J X, SHEN L, HONG Y L. Status and future scope of hydrogels in wound healing: synthesis, materials and evaluation[J]. Eur Polym J, 2020, 130: 109609.
[24] YANG Y T, LI M, PAN G Y, et al. Multiple stimuli-responsive nanozyme-based cryogels with controlled NO release as self-adaptive wound dressing for infected wound healing[J]. Adv Funct Mater, 2023, 33(31): 2214089.
[25] WEN M Y, WANG T Y, LI N, et al. Polyphenol-copper derived self-cascade nanozyme hydrogel in boosting oxygenation and robust revascularization for tissue regeneration[J]. Adv Funct Mater, 2024, 34(40): 2403634.
[26] QU J, ZHAO X, LIANG Y P, et al. Degradable conductive injectable hydrogels as novel antibacterial, anti-oxidant wound dressings for wound healing[J]. Chem Eng J, 2019, 362: 548-560.